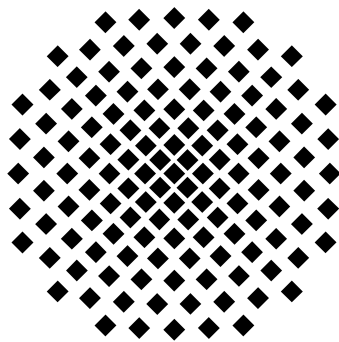


Characterization Of A Single Ion Detector In A Rydberg Experiment

bachelor thesis by Thomas Dieterle

October 5, 2015



PROF. DR. TILMAN PFAU
DR. SEBASTIAN HOFFERBERTH
5TH INSITUTE OF PHYSICS
UNIVERSITY OF STUTTGART

Declaration

I hereby declare that this thesis is my own work and that, to the best of my knowledge and belief, it contains no material previously published or written by another person, except where due acknowledgement has been made.

place date

signature

Contents

1	Introduction	1
2	Theoretical Background	3
2.1	Rydberg Atoms	3
2.2	DC - Stark Effect	3
2.3	Polarizability of Rydberg Atoms	5
2.4	Field Ionization of Rydberg Atoms	6
3	Experimental Setup	8
3.1	Electric Field Control	8
3.2	Micro-channel plate	10
3.3	FPGA based Time-Tagger	13
4	SIMION simulations	14
4.1	Electric field simulations	14
4.2	Ion trajectories	16
5	Ion Detection	20
5.1	Dark Counts of the MCP	20
5.2	Steering Voltage Scans	22
5.3	Detection Efficiency	25
5.4	Stark Maps and electric field calibration	31
5.4.1	Stark Map 100 D-state	31
5.4.2	Electric Field Calibration in 68 S-state	34
6	Summary and Outlook	36
7	Appendix	38
	References	40

1 Introduction

The recent progress in quantum optics allows the preparation, manipulation and detection of the quantum states of light on the few photon level. The radiation field is no longer considered to be an electromagnetic wave, but to consist of single particles, the photons. Rydberg atoms are a medium with excellent properties for generating and controlling quantum-optical states. These atoms are highly excited atoms where at least one electron is in a state whose principle quantum number n is significantly higher than the ground state. Especially alkali Rydberg atoms with properties similar to Hydrogen are feasible for working on the single atom and photon level.

The large polarizability of Rydberg atoms scaling with n^7 requires the control and compensation of external stray fields to achieve smaller linewidths of Rydberg energy levels and thus increase the stability of the experiment. Furthermore electric fields can be used to tune Rydberg energy levels yielding different interaction strengths and blockade radii [WS08]. If one atom is excited to a Rydberg-state, the energy levels of neighboring Rydberg atoms are shifted due to the strong interaction. This prevents them from excitation by the driving laser resulting in a radius of typically several micrometers in which only one Rydberg atom can be excited [LFC⁺01].

The ability not only to tune but to basically turn the interactions on and off as well as switching signs from attractive to repulsive makes Rydberg-atoms, together with high particle densities in ultra-cold atomic gases, a highly interesting candidate for applications in quantum-computation. The idea of a quantum computer, i.e a computational device based on quantum physics, was first proposed in the 1980s by Richard Feynman [FS82].

The utilization of Rydberg atoms to implement different gates for quantum-computation started to be proposed at the beginning of the 2000s [JCZ⁺00] [LFC⁺01]. All these proposals are based on the Rydberg-blockade effect. The first characterization of a cooperative optical nonlinearity by coupling a probe transition to a Rydberg state using electromagnetically induced transparency (EIT) has been published in 2010 [PMG⁺10]. In 2012 the first demonstration of quantum nonlinearities with single photons enabled by strongly interacting Rydberg atoms has been demonstrated [PFL⁺12].

These results emphasize the usage of Rydberg atoms as fundamental components for quantum-computational applications such as single-photon sources [DK12], single-photon absorbers [HLW⁺11] or quantum repeaters [ZMHZ10].

Most recently all optical switching with single photons based on Rydberg blockade effects [BTRD14] as well as an all-optical single photon transistor mediated by Rydberg interactions [GTS⁺14] could be realized paving the way towards enabling quantum memories.

During this thesis the detection of ionized Rydberg atoms with a micro-channel-plate (MCP) and the new electric field control integrated into the experiment have been characterized. A micro-channel-plate is a single ion detector that is able to detect ionized Rydberg atoms via secondary electron emission on the channel walls. The ability to ionize Rydberg atoms by applying electric field pulses with high amplitudes and guide

ions with adequate voltages allows the measurement of the number of created ions on a detector. With the integration of the micro-channel-plate to the experiment a second way of detecting Rydberg atoms has been introduced. This destructive way of detecting Rydberg atoms complements the non-destructive detection via transmission of a probe light field which is detected with single-photon-counting modules (SPCM).

The quadratic Stark effect occurring when the degeneracy of low l -states is lifted due to the quantum defect [LWN⁺12] can not only be used to simply tune energy levels but also to calibrate the electric field by taking Stark maps where either the Rydberg atoms energy level or the respective detuning are plotted against the varied electric field using the MCP to detect ions for different electric field strengths and detunings.

2 Theoretical Background

To motivate the necessity of precise control of electric fields this section describes the influence of electric fields on Rydberg atoms and its energy levels. First of all, Rydberg atoms with their general properties are introduced followed by a perturbative description of the DC - stark shift that specifies the shift of energy levels in small electric fields. Furthermore the properties of electric field ionization and polarizability of Rydberg atoms are mentioned.

2.1 Rydberg Atoms

Rydberg atoms are atoms where at least one electron is excited to a principle quantum number significantly higher than the ground state. In terms of classical Kepler radii the outer electron resides far away from the rest of the atom which is simply described by the core.

Since in alkali atoms only one valence electron is present, they are often used in Rydberg experiments. Further properties of especially alkali Rydberg atoms are described in the following sections.

2.2 DC - Stark Effect

The effect of small electric fields on Rydberg energy levels can be described quantum mechanically either by diagonalizing the full Hamiltonian or by a perturbative approach. This section introduces the Stark shift as its done most textbooks using perturbation theory [Sch07]. The influence of a small perturbation H_1 to the eigen-energies can be approximated by

$$E_{nlm} = E_{nlm}^0 + \langle n, l, m | H_1 | n, l, m \rangle + \sum_{n', l', m' \neq n, l, m} \frac{|\langle n, l, m | H_1 | n', l', m' \rangle|^2}{E_{nlm}^0 - E_{n'l'm'}^0} + \mathcal{O}(H_1^3) \quad (2.1)$$

E_{nlm} describes the eigen-energy of $|n, l, m\rangle$ in the perturbed system, E_{nlm}^0 the eigen-energy to the unperturbed Hamiltonian H_0 . The potential for a weak, homogeneous electric field is given by

$$\Phi = -\mathbf{E} \cdot \mathbf{r} \quad (2.2)$$

The perturbation H_1 for an atom placed in such an electric potential is then determined by

$$H_1 = e \cdot \Phi \quad (2.3)$$

It was assumed that the electron is charged with $-e$. Assuming then the electric field to point in z-direction the perturbation can be written as:

$$H_1 = e |\mathbf{E}| z \quad (2.4)$$

Hence the energy shift induced by the small electric field yields:

$$\Delta E_{nlm} = e|\mathbf{E}|\langle n, l, m | z | n, l, m \rangle + e^2|\mathbf{E}|^2 \sum_{n', l', m' \neq n, l, m} \frac{|\langle n, l, m | z | n', l', m' \rangle|^2}{E_{nlm}^0 - E_{n'l'm'}^0} \quad (2.5)$$

Although the sum on the right side of the equation appears to be complicated, the application of selection rules simplifies the sum as most of the matrix elements $\langle n, l, m | z | n', l', m' \rangle$ are zero. Since the angular momentum operator $L_z = xp_y - yp_x$ commutes with z it follows that

$$\langle n, l, m | [L_z, z] | n', l', m' \rangle = \langle n, l, m | L_z z - z L_z | n', l', m' \rangle \quad (2.6)$$

$$= \hbar(m - m') \langle n, l, m | z | n', l', m' \rangle = 0 \quad (2.7)$$

$$\rightarrow m' = m \quad (2.8)$$

A similar calculation for the commutator of $[L^2, z]$ leads to the selection rule $l' = l \pm 1$. For Rydberg atoms in low l-states (e.g s,p,d,f) the unperturbed energy-levels are no longer degenerate due to the quantum defect, that lifts the degeneracy as a result of its dependence on the total angular momentum quantum number j . In this case it is clear, that the first order term will not give any contribution to ΔE_{nlm} . This follows from simple symmetry arguments. Since the perturbation H_1 is given by an anti-symmetric function the expectation value $\langle n, l, m | z | n, l, m \rangle$ only leads to a finite value for states with different parity. Application of the selection rules then yields:

$$\Delta E_{n,l,m} = e^2|\mathbf{E}|^2 \sum_{n', l'=l+1} \frac{|\langle n, l, m | z | n', l', m \rangle|^2}{E_{nlm}^0 - E_{n'l'm}^0} \quad (2.9)$$

According to the selection rules, the terms that vary linearly with the electric field vanish and only quadratic terms survive. Hence, this type of energy-shift is called *quadratic* stark effect. Equation 2.9 can now be written by introducing the electric polarizability α .

$$\Delta E_{nlm} = -\frac{1}{2}\alpha|\mathbf{E}|^2 \quad (2.10)$$

Hence, the electric polarizability is given by

$$\alpha_{nlm} = 2e^2 \sum_{n', l'=l+1} \frac{|\langle n, l, m | z | n', l', m \rangle|^2}{E_{nlm}^0 - E_{n'l'm}^0} \quad (2.11)$$

The quadratic Stark effect can also be described in a classical picture that gives an intuitive understanding of the behaviour. In the low l-state case, the non-degenerate case, an external electric field leads to a displacement of the electrons probability density with respect to the core. This can be understood by inducing a dipole moment $\mathbf{p}_{\text{ind}} = \alpha\mathbf{E}$. The corresponding potential V_{dip} is given by $V_{\text{dip}} = -\mathbf{p}_{\text{ind}}\mathbf{E} = \alpha\mathbf{E}^2$. So even this simple approach shows the quadratic dependence of the energy shift on the electric field.

2.3 Polarizability of Rydberg Atoms

As the energy of Rydberg states, especially of alkali atoms, is well described by the Bohr atom picture, the binding energy is given by

$$E_{nlj} = E_{\infty} - \frac{R'}{(n - \delta_{nlj})^2} \quad (2.12)$$

where R' denotes the Rydberg constant, E_{∞} the ionization energy limit and $n^* = n - \delta_{nlj}$ the effective quantum number with δ_{nlj} as the quantum defect. The quantum defect has to be introduced, since the structure of alkali atoms is hydrogen-like, but yet deviates from a hydrogen atom due to the core electrons which add a repulsive Coulomb potential for the Rydberg electron.[LWN⁺12] A simple $1/r$ Coulomb potential is not applicable anymore which leads to the introduction of the quantum defect that alters the Rydberg formula as described in Equation 2.12.

With the given binding energy, the energy difference between adjacent n states scales $\propto n^{-3}$. Regarding Equation 2.11 the polarizability is proportional to the square of the dipole moment μ divided by the energy difference of adjacent n levels:

$$\alpha \propto \frac{\mu^2}{\Delta_n} = \frac{|\langle n, l, m | z | n', l', m \rangle|^2}{E_{nlm}^0 - E_{n'l'm}^0} \quad (2.13)$$

As the dipole moment μ scales with n^2 the polarizability of Rydberg atoms scales as n^7 .

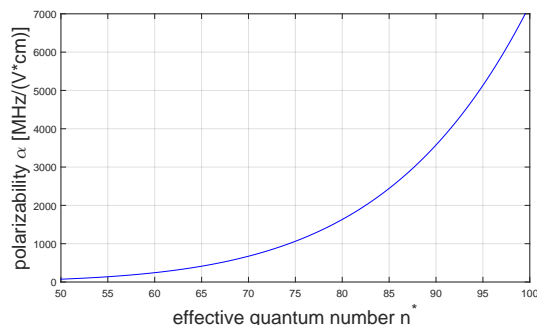


Figure 2.1: Dependence of the polarizability α on the effective principle quantum number n^* extracted from experimental data [OS85]. The results are in good agreement with perturbative calculations

Experimental data [OS85] with obtained values of α for different Rydberg states conform to the following function of n^* showing the n^{*7} dependence with a deviation $\propto n^{*6}$:

$$\alpha \left[\frac{\text{MHz}}{\text{Vcm}} \right] = 2.202(28) \cdot 10^{-9} n^{*6} + 5.53(13) \cdot 10^{-11} n^{*7} \quad (2.14)$$

To achieve a linewidth of for example 10 kHz in the 68 S state which has a polarizability of $217.4 \text{ MHz}/(\text{V}/\text{cm})^2$ the electric field fluctuations had to be smaller than $E = 0.0096 \text{ V}/\text{cm}$ showing that a precise control of external stray electric fields is necessary.

2.4 Field Ionization of Rydberg Atoms

As the previous section dealt with atoms in small electric fields, now high electric fields will be considered. For high electric field strengths the problem can be approached in a classical picture. The potential between the valence electron and the core of the Rydberg atom is of Coulomb type:

$$V_{\text{Coul}} = -\frac{e^2}{4\pi\epsilon_0 r} \quad (2.15)$$

As described in the previous section a homogeneous electric field pointing in z-direction leads to a potential of the form

$$V_E = -eEz \quad (2.16)$$

and as a result the outer electron of the Rydberg atom thus feels an effective potential which is given by

$$V_{\text{eff}} = -\frac{e^2}{4\pi\epsilon_0 r} - eEz \quad (2.17)$$

This effective potential shows a saddle point determined by

$$r_s = \sqrt{\frac{e}{4\pi\epsilon_0 E}} \quad (2.18)$$

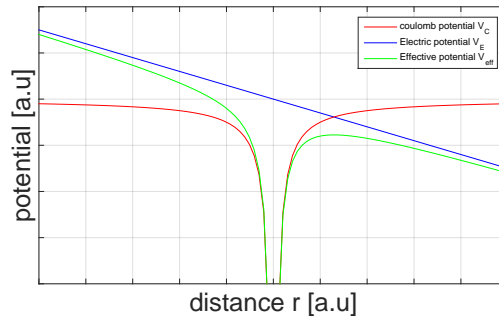


Figure 2.2: The classical coulomb potential $\propto -\frac{1}{r}$ (red) gets modified to an effective potential $\propto -\frac{1}{r} - E \cdot r$ (blue) by an electric potential $\propto -E \cdot r$. The modification of the potential leads to a saddle point. Rydberg electrons with a binding energy below the energy of the saddle-point can no longer be bound and get ionized

In the classical picture the valence electron is bound to Rydberg atoms core if the energy of the saddle-point is higher than the binding energy. If the binding energy is higher than the energy of the saddle-point the outer electron can no longer be hold and the Rydberg

atom gets ionized. It is now possible to estimate the electric field required to field ionize Rydberg atoms by simply comparing the binding energy of a Rydberg atom E_{ryd} to the energy of the saddle-point. With the condition

$$E_{\text{ryd}} \leq V_{\text{eff}}(r_s) \quad (2.19)$$

the minimum electric field to ionize a Rydberg atom is given by

$$|\mathbf{E}| \leq \frac{\pi\epsilon_0 R_{\text{ryd}}^2}{e^3 n^{*4}} \quad (2.20)$$

where R_{ryd} is the Rydberg constant and n^* the effective quantum number of the Rydberg atom. The dependence of the electric field required to ionize Rydberg atoms on the effective quantum number proportional to $\frac{1}{n^{*4}}$ shows that on the one hand low electric fields in the range of $\frac{\text{kV}}{\text{cm}}$ are sufficient to ionize high Rydberg states but on the other hand a state selective ionization of high Rydberg states gets more and more complicated and requires precise control of applied electric fields.

3 Experimental Setup

This section deals with the relevant parts of the experimental setup used during the work of this thesis. First the electric field control is described followed by an introduction of the working principle of the MCP and its characteristics. Finally the FPGA-based Time-Tagger to count the MCP pulses is briefly introduced.

3.1 Electric Field Control

The design and realization of the electric field control is described in [Sch14]. The whole electric field control was developed to compensate external stray fields as well as to tune the energy levels of Rydberg atoms.

The design was realized in a cloverleaf configuration as shown in Figure 3.1 with 8 electrodes (numbers 1 to 8) that can be addressed individually. Electrodes 9 and 10 are chosen to guide ionized Rydberg atoms towards the detector, electrode 11 supplies the mesh in front of the MCP which was designed to shield stray electric fields resulting from high voltages applied to the MCPs front and back plate. Number 12 and 13 denote the MCPs front and back plate.

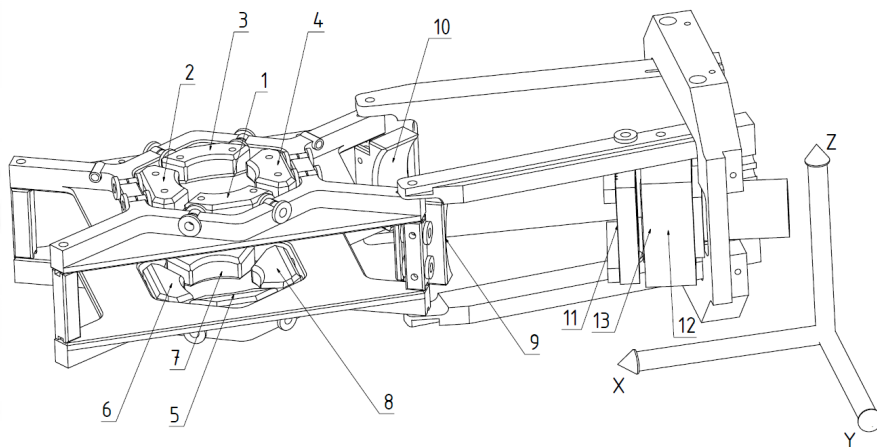


Figure 3.1: Autodesk Inventor drawing of the electric field control with 8 independent electrodes in a cloverleaf configuration and two electrodes to guide ionized Rydberg atoms. 11-13 denote mesh and MCP.

Figure 3.2 shows schematically how the voltages on the individual plates are generated and controlled.

The field plates 1-8 except electrodes 2 and 6 are integrated into the experiment control using a 8 channel USB analog high-drive voltage source. Electrodes 2 and 6 as well as the steering electrode 9 and the supply for the mesh in front of the MCP are controlled using a 16 channel analog box.

The required voltages up to 500 V for electrodes 2 and 6 as well as for electrode 9 are provided by two high voltage sources from AppliedKilovolts. The voltage sources are then connected to a HV-switch whose output leads to the feedthroughs in the steel octagon. Between the output of the voltage source and the HV-switch, RC-circuits with $22\ \mu\text{F}$ capacitors and $50\ \text{k}\Omega$ resistors were integrated as depicted in Figure 3.2. The constant output loads the capacitors which serve as a buffer to achieve more constant amplitude pulses. The resistors were chosen such that the discharge of the capacitors is fast enough to change ionization and steering voltages during an experimental sequence.

The MCP supply is provided via another high voltage source from AppliedKilovolts. The control voltage is set permanently to 9.4 V delivered by a bench power supply.

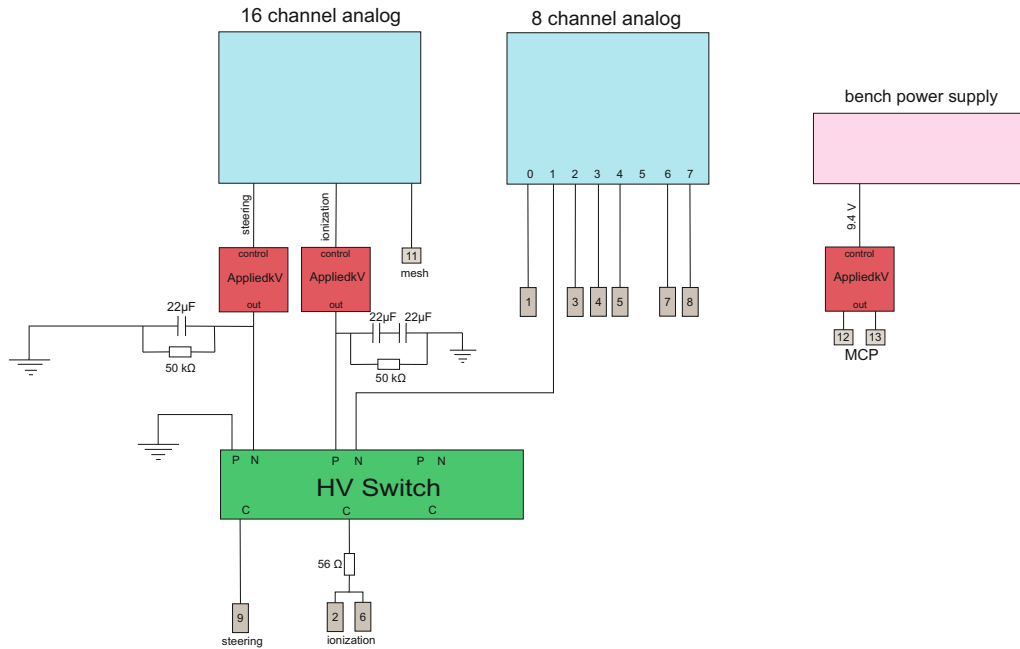


Figure 3.2: Schematic drawing and allocation of control voltages on the individual field plates.

3.2 Micro-channel plate

The detection of ionized Rydberg atoms is realized with a micro-channel-plate (MCP). Alternatively a channel electron multiplier, short channeltron, could be used to detect Rydberg ions.

A micro-channel plate consists of a huge amount of ultra-thin conductive glass capillaries, usually in the range of one to ten millions. These glass capillaries range from 4 to 25 μm in diameter and 0.2 to 1.0 mm in length and are fused together and sliced in the shape of a thin plate. Figure 3.3 shows the structure of a micro-channel plate with its glass capillaries. Each of these so called channels has the function of an electron multiplier where every channel of the MCP acts independently.

Together they form a two-dimensional secondary electron multiplier as the inside wall of every channel is built to have a specified resistance. When an electron, ion or other sources of radiation enter one of the channels, secondary electrons are emitted from the channel wall. These electrons are now accelerated by an electric field arising from a voltage applied to both end faces of the MCP. While traveling along their parabolic trajectories these electrons strike the opposite wall and thereby produce other secondary electrons to be emitted. In the sense of an electron multiplier this process is repeated several times along the channel leading to a large number of electrons at the output side. This behaviour is illustrated in Figure 3.4.

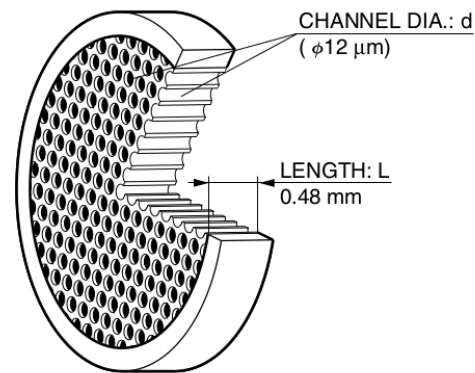


Figure 3.3: Structure and operating principle of micro-channel plates [Ham]

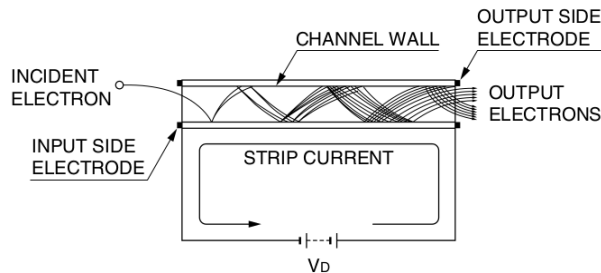


Figure 3.4: Operating principle of the MCP: an incident electron striking the channel wall and producing a secondary electron which also follows a parabolic trajectory due to the electric field applied between the MCP channel electrodes. This process is repeated several times leading to a large amount of output electrons.

Regarding the description of the MCPs working principle it is clear, that the thickness of a MCP is nearly equal to the length of a channel. A characteristic value is indicated by the ratio of channel length to channel diameter α which determines the gain of the MCP together with the inherent secondary emission factor of the channel wall material. Another characteristic is given by the bias angle which is formed by the channel axis with respect to the axis perpendicular to the plate surface. This angle has to be chosen such that the radiation detection efficiency reaches a maximum value and to prevent effectiveness of incident particles from passing through the channels. Usually bias angles vary between 5° to 15° .

The gain of the MCP is approximately given by $g = e^{G \cdot \alpha}$, where G gives the secondary emission characteristics of the channel wall. This factor is called the gain factor. α describes the mentioned ratio between length and diameter of one channel. The formula predicts that an increase of α results in a higher gain. Unfortunately it is not possible to make the gain arbitrary large. This is due to the fact that when the gain reaches a critical value, the noise increase caused by ion feedback becomes significantly larger. The phenomenon of ion feedback can be explained as follows:

When the MCP is operated at high gain, the residual gases are ionized inside the channels and these ions travel backward to the MCP input side. A large secondary pulse then may be generated as noise, eventually causing a discharge in the worst case.

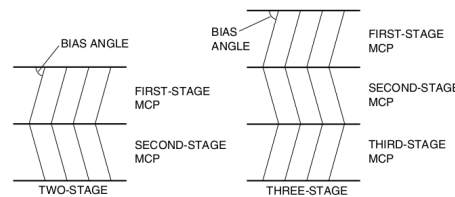


Figure 3.5: Cross section of a two stage and three stage MCP assembly indicating the bias angle between channel axis and the axis perpendicular to the plates surface

If higher gains are required, there is the possibility to use two-stage or even three-stage MCPs where two or three MCPs are used in stacked configurations. Such configurations are illustrated in Figure 3.5.

To minimize ion feedback effects in this configuration the bias angle of two adjacent stages is opposed. If residual gas atoms or molecules are ionized in the MCP channels by the multiplied electrons, this ionization causes false signals as the ions travel back to the MCP input side along the electric field. However, if the bias angle is opposed between two stages the generated ions get absorbed at the junction between every stage.

The micro-channel plate used in the experiment is the F4655-13 from Hamamatsu. To supply the front and back plate of the MCP, high voltage supplies from AppliedKilovolts are used. A home-built voltage divider made of high power resistors is used to get the required -2000 V at the MCP front plate and - 500 V at the MCP back plate. The voltage

supplies control the output voltage with a voltage between 0 V and 10 V. A lab voltage supply delivers the required supply voltage of 24 V.

To amplify the MCP signal and therefore to make it more feasible for counting single events with the FPGA based Time-Tagger described below, the operational amplifier ZX60-14012L-S+ from Mini-Circuits is used. This is a broadband amplifier from 300 kHz to 16 GHz with a maximum gain up to 11 dBm. Figure 3.6 shows some random MCP traces after being amplified with the ZX-14012L-S+. The mean pulse height is 0.321 V with a mean pulse width of 1.2164 ns. The minimum pulse width also determines the required bandwidth showing that the use of a broadband amplifier with up to 16 GHz is suitable to prevent any deforming of the pulses due to bandwidth limits.

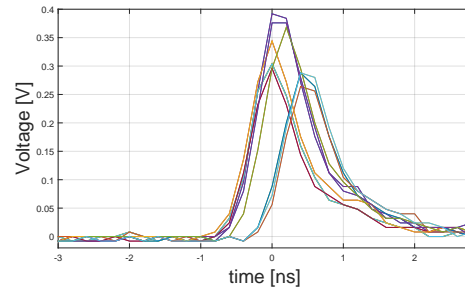


Figure 3.6: MCP traces from random events with amplifier ZX-14012L-S+ from MiniCircuits

3.3 FPGA based Time-Tagger

To count the analog pulses emitted by the MCP and amplified like it is explained above, a field-programmable gate array (FPGA) based Time-Tagger is in use. The module was developed in the 3rd physical institute by the group of Dr. H. Fedder. Its purpose is the time-resolved counting of digital pulses. In the experiment the Time-Tagger is used for the MCP signal as well as for the single photon counting modules.

The Time-Tagger consists of 8 independent channels with a time resolution of 60 ps. In case of the MCP signal one channel is used to trigger the Time-Tagger whereas a different channel is used to actually count pulses during the trigger pulse.



Figure 3.7: FPGA based Time-Tagger with 8 independent channels for time-resolved counting of digital pulses

The Time-Tagger is controlled via python, several control programs were developed in the 3rd institute as well as in the 5th institute.

Before integrating the MCP signal to the experiment control, several measurements were done to investigate dark count rates and required trigger levels. The Time-Tagger was therefore operated in a pulsed mode.

This mode measures counts per bin on a particular 'count' channel for a specified number of bins after a trigger on a different 'shot' channel. One trigger fills one line of a two dimensional array. The number of lines in the array can be set by 'number of shots'. Once this number has been reached, the next trigger moves back to the first line. Multiple runs through the array are added, not averaged. The option 'number of shots' specifies the number of repetitions and the counts for every new trigger pulse are written in a new line. The resulting output gives a matrix with dimensions (number of shots)x(number of bins).

For further evaluation the data is loaded with MATLAB. To trigger the Time-Tagger the Agilent 33522A wavefunction generator was used in burst mode, so that the instrument outputs a waveform (e.g. TTL-pulse) for a specified number of cycles. The function generator was also controlled via python using the SCPI programming language.

4 SIMION simulations

With the program SIMION electric fields originated from the voltages on different electrodes can be simulated as well as ion trajectories. The results of these simulations will be discussed in the following.

4.1 Electric field simulations

The figures below show simulated electric fields for different cases of applying voltages on electrodes 1 to 8. In every case, the MCP front plate was set to -500 V and the MCP back plate was set to -2000 V. The mesh in front of the MCP was set to -0.05 V. The origin of the coordinate system used below is defined by the position of the atom cloud. The figures show cuts of the electric fields in different planes cropping an area around the atomic cloud.

The simulated electric fields with electrode configurations as described in Figure 4.1 to Figure 4.3 lead to conversion factors to generate a desired electric field in a particular direction.

1. Electric field in x-direction using electrodes 4 and 8 with positive polarity and electrodes 2 and 6 with negative polarity:

$$E(U) \left[\frac{\text{V}}{\text{cm}} \right] \cong 0.350 \frac{1}{\text{cm}} \cdot U[\text{V}] \quad (4.1)$$

2. Electric field in y-direction using electrodes 1 and 5 with positive polarity and electrodes 3 and 7 with negative polarity:

$$E(U) \left[\frac{\text{V}}{\text{cm}} \right] \cong 0.410 \frac{1}{\text{cm}} \cdot U[\text{V}] \quad (4.2)$$

3. Electric field in z-direction using electrodes 1 and 3 with positive polarity and electrodes 5 and 7 with negative polarity:

$$E(U) \left[\frac{\text{V}}{\text{cm}} \right] \cong 0.398 \frac{1}{\text{cm}} \cdot U[\text{V}] \quad (4.3)$$

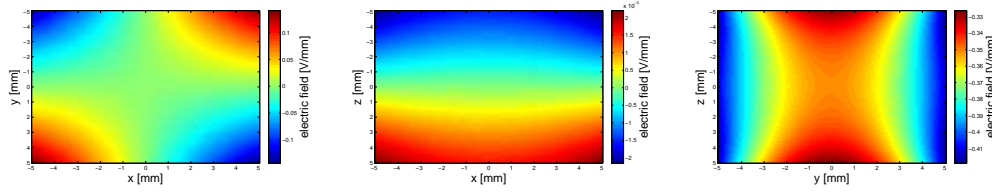


Figure 4.1: Electric fields generated by setting a positive voltage on electrodes 2 and 6 and a negative voltage on electrodes 4 and 8

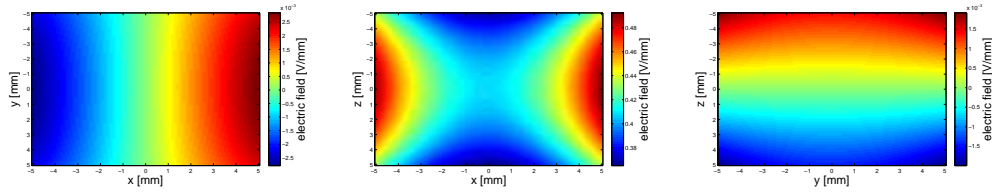


Figure 4.2: Electric fields generated by setting a positive voltage on electrodes 1 and 5 and a negative voltage on electrodes 3 and 7

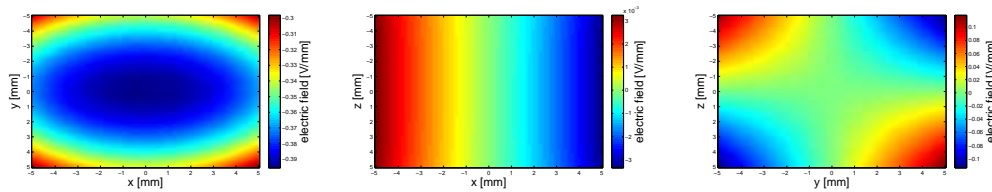


Figure 4.3: Electric fields generated by setting a positive voltage on electrodes 1 and 3 and a negative voltage on electrodes 5 and 7

Figure 4.1 to Figure 4.3 illustrate simulated fields in particular coordinate directions. The plotted area is much larger than the actual area of interest given by the size of the atom cloud. Although it has to be mentioned that the relative deviation, e.g. for applying a linear field in x-direction, over a volume of 1 mm^3 is about 1.4 %. It is not possible to create perfect homogeneous fields with this arrangement of the field plates. Only a parallel-plate condensator with two field plates could ensure a perfect linear field but can of course not be utilized in the existing experimental setup. However, the electric field simulations show that it is possible with the usage of four opposing electrodes to create nearly homogeneous electric fields over the area of interest given by the size of the atom cloud.

4.2 Ion trajectories

Despite the simulation of electric fields, ion trajectories were simulated using SIMION. The trajectory simulations were implemented with typically between 1 and 100 $^{87}\text{Rb}^+$ ions distributed in a sphere with a diameter in the range of the MOT size to get an idea of the distribution of ions on the MCP. An example for such a simulation can be seen in Figure 4.4.

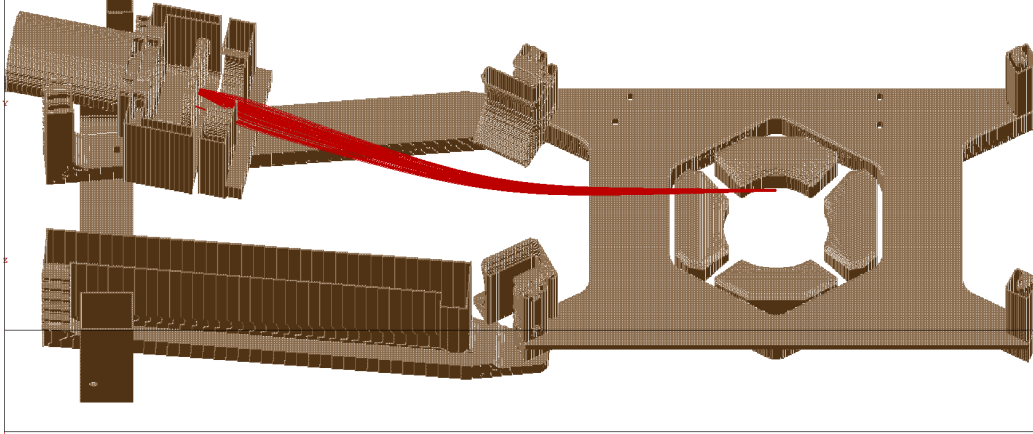


Figure 4.4: Simulated ion trajectory for 100 $^{87}\text{Rb}^+$ ions distributed in a sphere with a diameter of 200 μm in the center of symmetry. The ionization voltage on electrodes 2 and 6 was set to +500 V, the steering voltage on electrode 9 to -100 V.

Due to the experimental setup, the ionized atoms have to fly on a curved trajectory to hit the MCP which is achieved by setting an appropriate voltage on electrode 9. Electrode 10 could give us one more degree of freedom for example to achieve a spreading of the ions impinging the MCP. The deflection of ions achieved with a negative voltage on electrode 9 also leads to a spreading based on the size of the atomic cloud.

Apart from that, the dependence of the ion trajectories on an external magnetic field was investigated. Therefore a constant magnetic field heading in y -direction was implemented into the simulation of SIMION. Additionally a rough estimation of the influence on the trajectory by a Lorentz force can be made. Assuming that the electric energy gets fully translated into kinetic energy of the atoms, one can estimate their velocity.

$$E_{el} = E_{kin} \quad (4.4)$$

$$q \cdot E \cdot d = \frac{m \cdot v^2}{2} \quad (4.5)$$

$$\rightarrow v = \sqrt{\frac{2 \cdot E \cdot d \cdot q}{m}} \quad (4.6)$$

E denotes the absolute value of the electric field, m the mass of ^{87}Rb and d the distance

between atomic cloud and MCP. With the estimated velocity the acceleration due to the Lorentz force can be determined. In this estimation only the absolute value of the force has been taken into account.

$$F_L = q \cdot v \cdot B \quad (4.7)$$

$$\rightarrow a = \frac{F_L}{m} = \frac{q \cdot v \cdot B}{m} = \frac{q \cdot \sqrt{\frac{2 \cdot E \cdot d \cdot q}{m}} \cdot B}{m} \quad (4.8)$$

Finally the acceleration can be used to estimate the vertical deflection due to the magnetic field.

$$s = \frac{1}{2} \cdot a \cdot t^2 = \frac{1}{2} \cdot \frac{q \cdot \sqrt{\frac{2 \cdot E \cdot d \cdot q}{m}} \cdot B}{m} \cdot t^2 \quad (4.9)$$

t denotes the time of flight between atomic cloud and MCP which can be evaluated with SIMION. With a magnetic field $B = 4$ G, an electric field of $E = 1.85 \frac{\text{V}}{\text{mm}}$, a distance between opposed electrodes of $d \approx 50$ mm and a time of flight $t = 18 \mu\text{s}$, this leads to a vertical deflection of $s = 1.28$ mm which is negligible compared to the diameter of the MCP itself.

Similar results with even smaller deflections could be reproduced using SIMION.

Time of Flight Changing the ionization voltage leads to different times of flight of accelerated Rydberg ions. These flight-times are an important point when it comes to time the ionization pulses. Therefore the times of flight for different ionization voltages were recorded for every simulated particle and the mean arrival time has been calculated. Table 4.1 shows mean flight times for different ionization voltages. Additionally the value for the steering voltage was added due to the effect that it has to be adjusted for different ionization voltages. When it comes to ionize Rydberg atoms without considering any state selective ionization the full 500 V can be used to keep the time during different ionization pulses as short as possible and therefore increase the repetition rate in the experiment cycle.

U_{ion} [V]	$U_{steering}$ [V]	\bar{t}_{TOF} [μs]
100	-20	18.7
200	-40	13.5
300	-65	10.7
400	-80	9.3
500	-10	8.7

Table 4.1: mean flight times for different ionization voltages

Working with few or even single Rydberg atoms requires a high detection efficiency of ions on the MCP. The SIMION software can not only be used to record flight times of particles but also to record creation points as well as end coordinates of ions impinging the MCP.

Therefore 100 $^{87}\text{Rb}^+$ ions distributed in a sphere of approximately the size of the atom cloud were ionized and accelerated with + 100 V on electrodes 2 and 6. This voltage is just above the ionization threshold of Rydberg atoms in the 68 S state which will be used in the experiment.

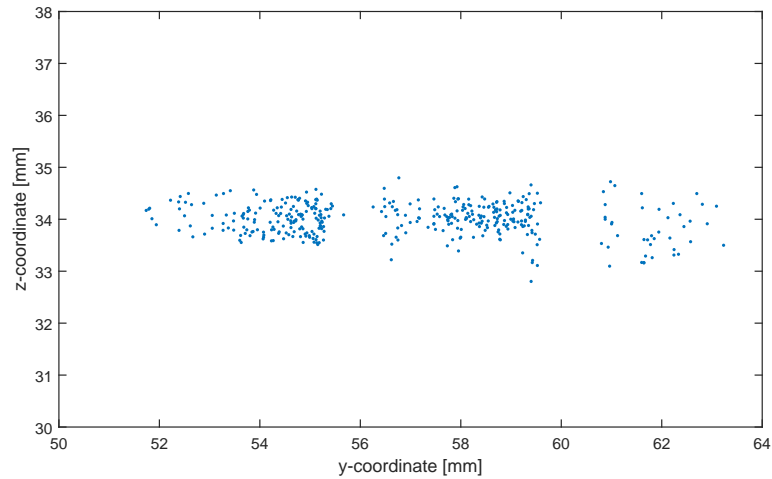


Figure 4.5: Simulated hit statistics of ions impinging the MCP. For the simulation 100 $^{87}\text{Rb}^+$ ions distributed in a sphere of the size of the atom cloud were used. The ionization voltage was chosen to be +100 V. The coordinates are SIMION coordinates.

Figure 4.5 shows the simulated hit-points of ions on the MCP in the y-z-plane. This plane includes the surface of the MCP except the MCP is tilted by a small angle which does not affect the purpose of this simulation. The simulated data contains three sets of 100 ions that were accelerated with + 100 V but deflected with different voltages for the steering electrode. The hit-points of all sets of ions are distributed in a range of 12 mm in y-direction. For a single set of ions the horizontal spreading is in the range of 4 mm which is about a third of the detection area of the MCP with a diameter of 13 mm. In z-direction the ions are distributed over a much smaller area.

The expansion of ions in the horizontal direction mostly depends on the size of the atom cloud assumed for the simulation but also on the voltage applied to ionize and guide the particles.

However this simulation indicates that the wide spreading in y-direction prevents a saturation due to the dead time of a particular channel as well as the risk of aging effects or even destruction of single channels if the ions would only be distributed over a bunch of channels. It is also clear that by adjusting the voltage for the steering electrode, used MCP channels can be controlled.

5 Ion Detection

This section deals with first characterization measurements of the MCP concerning dark count rates and required trigger levels, followed by the first actual ion detection and optimization of steering voltages. Furthermore the ion detection efficiency is estimated and Stark maps are recorded to calibrate stray electric fields.

5.1 Dark Counts of the MCP

Dark counts are caused by several different factors. MCP dark counts originate from electric field emission from the channel walls as well as from ionization of residual gases. Furthermore local discharge by a high electric field or photo-electron emission by photons are possible sources that increase the dark count rate of the MCP.

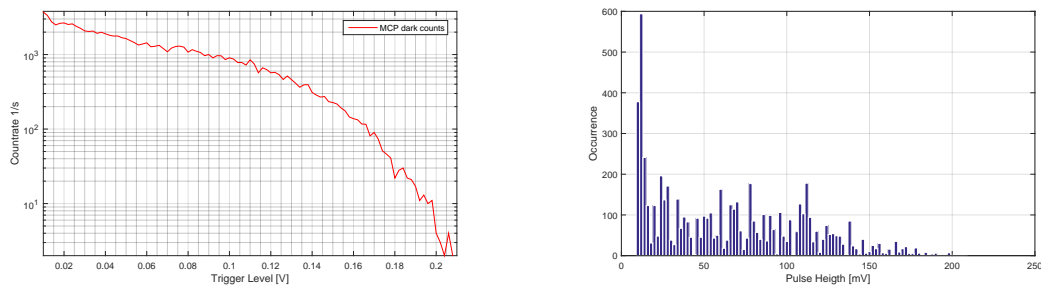
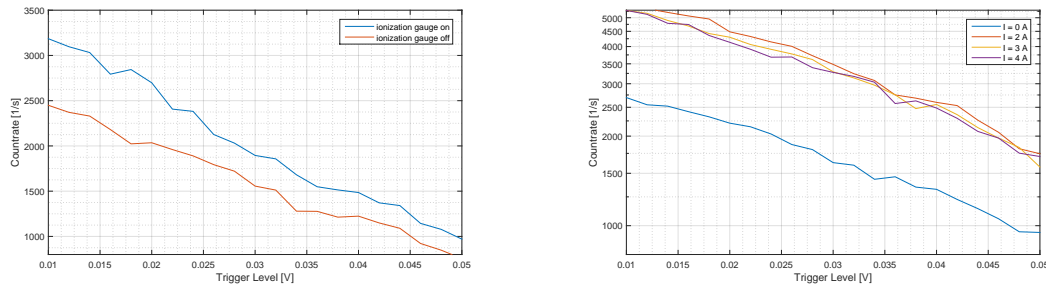


Figure 5.1: MCP dark counts for different trigger levels (left) and MCP pulse-height-distribution (right)

Figure 5.1 shows dark counts of the MCP for different trigger levels levels (left) as well as the resulting pulse height distribution (right).

The trigger level for further working with the MCP is chosen to 20 mV which minimizes missing ion counts. Lower trigger levels are not recommendable due to electrical noise that causes a false increase of the MCP count rate. The Time-Tagger was actually built for digital TTL-pulses and not for analog pulses like the MCP signal. To be nevertheless able to use it for our purpose the trigger level has to be set extremely low.

The pulse height distribution was calculated by iteratively evaluating the difference in occurrences for adjacent trigger levels. At trigger levels below 15 mV the pulse height distribution shows a high increase in occurrences which is a clear indication that electrical noise falsifies the counting signal. This can be simply prevented by setting a higher threshold for the trigger level.



(a) influence of the ionization gauge on the count rate (b) influence of the Rb dispensers on the count rate

Figure 5.2: count rate at low trigger levels to investigate the influence of Rb dispensers and ionization gauge on the dark count statistics

With the Rb-dispensers in place their influence on the dark count rate was studied as well as the influence of the ionization gauge which is used for low pressure respectively vacuum measuring.

Figure 5.2a and Figure 5.2b show that for low trigger levels, that will be set in the experiment, both elements have an effect in increasing the dark count rate.

As the ionization gauge works as a hot cathode-gauge a regulated electron current is emitted resulting in collisions of electrons with residual gas molecules.

For trigger levels between 10 mV and 50 mV the mean count rate increases by 25.8 % in consequence of a powered ionization gauge.

The effect of the Rb-dispensers is even more significant. The powered dispensers cause an increase of dark counts of 51.28 % averaged over different operating currents and trigger levels between 10 mV and 50 mV. Surprisingly, a different operating current has no remarkable influence on the dark count rate.

Although both elements clearly influence the number of occurrences, dark count rates in the kHz-regime are sufficiently low compared to the timescale of a few μs where the Time-Tagger gets triggered and therefore counts are measured.

5.2 Steering Voltage Scans

The attempt of first detection measurements was on the one hand to first detect actual ionized Rydberg atoms but also to optimize voltages that have to be set for different ionization voltages on the steering electrode.

Therefore the steering voltage was iterated recording the MCP signal for a constant ionization voltage. This procedure was repeated for different ionization voltages.

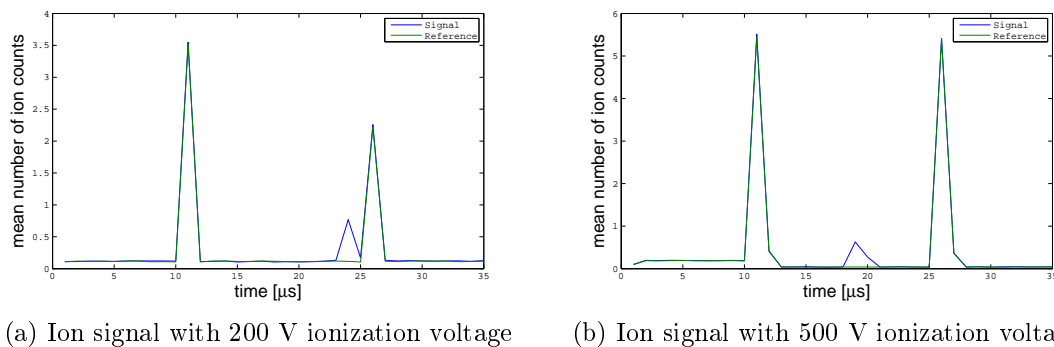
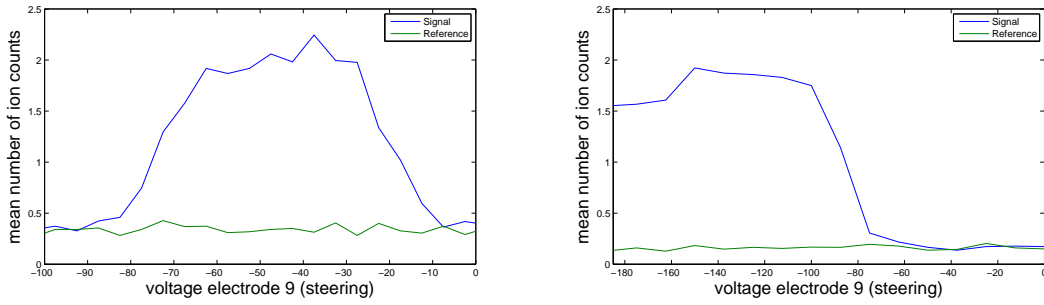


Figure 5.3: Ion signal for two different ionization voltages. The two high peaks are a crosstalk signal resulting from the voltage applied to ionize Rydberg atoms. The actual ion signal is given by the small peak between the crosstalk.

Figure 5.3a and Figure 5.3b show the time resolved ion signal for two different ionization voltages. In the experiment cycle the ionization time, the time between turning on and off the HV-switch, was set to $15 \mu\text{s}$. As already mentioned in subsection 5.1 local discharge from high electric fields can cause dark counts on the MCP. This crosstalk signal is depicted in both figures with a time difference of $15 \mu\text{s}$ clearly showing the relation to the ionization pulses. Furthermore this crosstalk signal is equal for both signal and reference shot. The actual ion signal is given by the small peak between the ionization pulses where signal and reference shot differ. For any further evaluation only the time bins corresponding to the actual ion signal were used.

In subsection 4.2 flight times for different ionization voltages were determined using the SIMION software. The magnitude of these could also be reproduced with Figure 5.3a and Figure 5.3b. One should point out that the ion signal depicted in the figures is an average signal. Summing and averaging the ion signal for many shots leads to a smearing of the pulse that can be seen in both figures. However, the time difference between ionization pulse and ion signal clearly differs for both ionization voltages reproducing the magnitude of the simulations with the SIMION software.



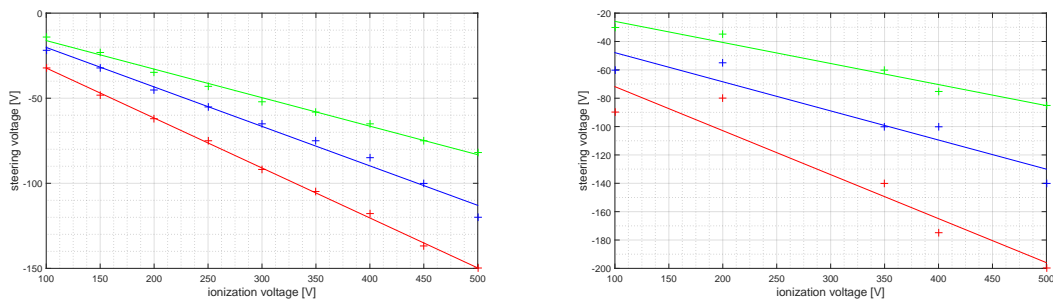
(a) Steering voltage scan with 200 V ionization voltage (b) Steering voltage scan with 500 V ionization voltage

Figure 5.4: Ion signal for two different scans of the steering voltage.

Figure 5.4a and Figure 5.4b illustrate the MCP ion signal for different steering voltages at constant ionization voltages of 200 V and 500 V respectively. Both scans confirm the expected behaviour. At a certain voltage for the steering electrode ions start impinging the detection area of the MCP. The ion signal then flattens remaining at a constant level within statistical fluctuations.

Figure 5.5a shows required steering voltages for different ionization voltages between 100 V and 500 V in steps of 50 V. This data results from trajectory simulations with SIMION. The resulting steering voltages were fitted with a linear function. The three fits correspond to different hit points on the MCP. The green fit curve denotes ions that hit the left edge of the MCP detection area, the red fit curve ions that hit the right edge of the MCP detection area. The blue fit corresponds to ions impinging the center of the MCP detection area.

Figure 5.5b shows actually applied steering voltages for different ionization voltages. The data points were calculated by taking a threshold which was chosen as half of the maximum ion signal and identifying the corresponding steering voltage. These two values determine the required voltages for ion hits on the left edge and on the right edge of the MCP detection area. The MCP center was determined by taking the maximum ion signal.



(a) SIMION simulated data for required steering voltages (b) experimental data to reproduce the simulations

Figure 5.5: Three linear fits for different impinging points on the MCP.

Green: ions impinging left side of MCP, red: ions impinging right side of MCP, blue: ions impinging center of MCP

Table 5.1 summarizes the obtained values of steering voltages for different ionization voltages to make the simulation better comparable with the experimental data. It would have been surprising if the simulations could be more or less reproduced one-to-one in the experiment. However in particular for high ionization voltages the agreement of experimental data with the simulations is remarkably good.

The highest discrepancy occurs for the obtained values of ions that hit the right edge of the MCP detection area. In the experiment even higher voltages could be applied still impinging the MCP and producing an ion signal. This fact is a good property as a precise setting of the steering voltage is not required to produce a maximum ion signal as long the voltage stays within the presented range. This deviation from the theoretical values can occur because the MCP is mounted in a slightly different angle to the specification in the Autodesk Inventor design data. In the actual setup the angle of the MCP is not exactly fixed and therefore the MCP might be slightly shifted.

V_{ion} [V]	Simulated data			Experimental data		
	V_l [V]	V_m [V]	V_r [V]	V_l [V]	V_m [V]	V_r [V]
100	-14	-22	-32	-30	-60	-90
200	-35	-45	-62	-35	-55	-80
350	-58	-75	-105	-60	-100	-140
400	-65	-85	-120	-75	-125	-175
500	-80	-120	-150	-85	-140	-200

Table 5.1: Comparison of simulated and experimental steering voltages for different ionization voltages. V_i denote voltages required for different hit-points on the MCP with $i = l, m, r$ standing for left, middle and right.

5.3 Detection Efficiency

The idea behind the determination of the ion detection efficiency was the estimation of the average number of produced Rydberg excitations. The exact approach will be discussed in the following. First of all the physical properties of an atomic three-level-system shall be discussed. Figure 5.6 depicts an atomic three-level-system in a ladder-scheme. This scheme will be used to introduce the physical description of a three level system [FIM05] and it will be the configuration for the Rydberg excitation in the experiment.

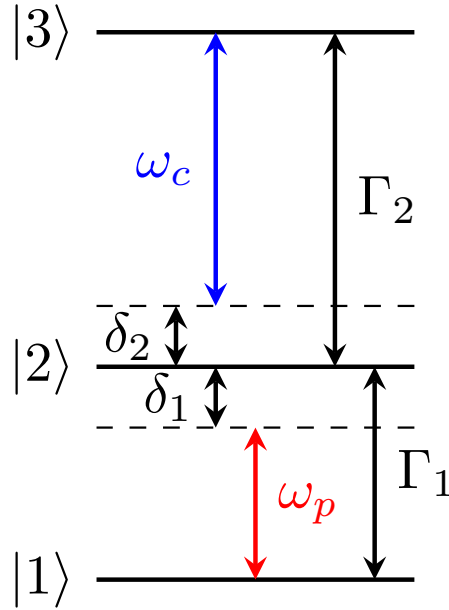


Figure 5.6: Ladder-type atomic 3-level system used in the experiment. The ground state $|1\rangle$ is given $5 S_{1/2}$, the $5 P_{3/2}$ level is used for the intermediate state $|2\rangle$ and the $66 S$ or $68 S$ for the Rydberg state $|3\rangle$.

The transition between the states $|1\rangle$ and $|3\rangle$ is typically dipole forbidden. The highest energy state $|3\rangle$ is of opposite parity to $|1\rangle$ and $|2\rangle$ and has a non-zero electric dipole coupling to both states. The transition between $|1\rangle$ and $|2\rangle$ is driven by the external probe laser field with frequency ω_p which is nearly in resonance with the atomic transition. The detuning between the resonance of both states $|1\rangle$ and $|2\rangle$ is given by δ_1 .

The transition between $|2\rangle$ and $|3\rangle$ is driven by the coupling field with frequency ω_c . The detuning from resonance is determined by δ_2 . States $|2\rangle$ and $|3\rangle$ will be treated with a finite lifetime and decay with the rates Γ_1 and Γ_2 into states $|1\rangle$ and $|3\rangle$, respectively.

Within the dipole approximation the atom laser interaction is typically expressed in terms of the Rabi frequency $\Omega = \boldsymbol{\mu} \cdot \mathbf{E}_0 / \hbar$ where \mathbf{E}_0 denotes the amplitude of the electric field \mathbf{E} and $\boldsymbol{\mu}$ the transition electronic dipole moment. After introducing the rotating-wave approximation where rapidly oscillating terms with frequency $\omega_p + \omega_c$ can be neglected and transforming into a rotating frame the Hamiltonian \hat{H}_{int} of the three-level atom

interacting with a coupling laser with Rabi frequency Ω_c and a probe laser field with Rabi frequency Ω_p and the density matrix $\hat{\rho}$ can be written as:

$$\hat{H}_{int} = -\frac{\hbar}{2} \begin{pmatrix} 0 & 0 & \Omega_p \\ 0 & 2(\delta_1 - \delta_2) & \Omega_c \\ \Omega_p & \Omega_c & 2\delta_1 \end{pmatrix} \text{ and } \hat{\rho} = \begin{pmatrix} \rho_{11} & \rho_{12} & \rho_{13} \\ \rho_{21} & \rho_{22} & \rho_{23} \\ \rho_{31} & \rho_{32} & \rho_{33} \end{pmatrix} \quad (5.1)$$

In a semi-classical picture the probe and coupling field are treated classically with small detunings δ_1 and δ_2 to their respective Rabi frequencies Ω_p and Ω_c . The atomic interaction Hamiltonian is then introduced with

$$\hat{H}_{int} = -\frac{\hbar}{2} \left(\Omega_p(t) \hat{\sigma}_{31} e^{i\delta_1 t} + \Omega_c(t) \hat{\sigma}_{32} e^{i\delta_2 t} \right) + c.c. \quad (5.2)$$

where $\hat{\sigma}_{ij} = |i\rangle\langle j|$ is the atomic projection operator and *c.c.* the complex conjugate of both terms in brackets. The dynamics of the laser-driven atomic three level system are governed by the master equation for the atomic density operator $\hat{\rho}$. Involving damping terms in the von-Neumann equation one obtains the following master equation for the three level system:

$$\begin{aligned} \frac{\partial \hat{\rho}}{\partial t} = & -\frac{i}{\hbar} [\hat{H}, \hat{\rho}] + \frac{\Gamma_1}{2} (2\hat{\sigma}_{13} \hat{\rho} \sigma_{31} - \hat{\sigma}_{33} \hat{\rho} - \hat{\rho} \hat{\sigma}_{33}) \\ & + \frac{\Gamma_2}{2} (2\hat{\sigma}_{23} \hat{\rho} \sigma_{32} - \hat{\sigma}_{33} \hat{\rho} - \hat{\rho} \hat{\sigma}_{33}) \\ & + \frac{\gamma_{2d}}{2} (2\hat{\sigma}_{22} \hat{\rho} \sigma_{22} - \hat{\sigma}_{22} \hat{\rho} - \hat{\rho} \hat{\sigma}_{22}) \\ & + \frac{\gamma_{3d}}{2} (2\hat{\sigma}_{33} \hat{\rho} \sigma_{33} - \hat{\sigma}_{33} \hat{\rho} - \hat{\rho} \hat{\sigma}_{33}) \end{aligned} \quad (5.3)$$

The second and third term on the right-hand side of the equation describe spontaneous emission from state $|3\rangle$ to states $|1\rangle$ and $|2\rangle$ with rates Γ_1 and Γ_2 respectively. In the last two terms energy-conserving dephasing processes with rates γ_{2d} and γ_{3d} have been introduced.

In general this master equation can only be solved numerically. However, in the weak probe limit ($\Omega_p \ll \Omega_c$), an analytic solution for the linear susceptibility can be obtained by taking $\rho_{11} \approx 1$ and using a rotating frame to eliminate fast exponential time dependences:

$$\chi^{(1)} = \frac{|\boldsymbol{\mu}_{13}|^2 \cdot \varrho}{\varepsilon_0 \hbar} \cdot \left[\frac{4\delta(|\Omega_c|^2 - 4\delta\Delta) - 4\Delta\gamma_{21}^2}{||\Omega_c|^2 + (\gamma_{31} + i2\Delta)(\gamma_{21} + i2\delta)|^2} + i \frac{8\Delta^2\gamma_{31} + 2\gamma_{21}(|\Omega_c|^2 + \gamma_{21}\gamma_{31})}{||\Omega_c|^2 + (\gamma_{31} + i2\Delta)(\gamma_{21} + i2\delta)|^2} \right] \quad (5.4)$$

with the single-photon detuning $\Delta = \delta_1$ and the two photon detuning $\delta = \delta_1 - \delta_2$. Furthermore $\gamma_{31} = \Gamma_1 + \Gamma_2 + \gamma_{3d}$ and $\gamma_{21} = \gamma_{2d}$. In this case ϱ denotes the atomic density. To observe the state of the atom two different detection methods are used. Rydberg ionization and detection with the MCP destroy the excitation. A non-destructive detection is realized via observation of the light field interacting with the atoms in the cloud which

is then detected by the single photon counting modules (SPCM). The amount of light which is transmitted through the absorbing medium is given by the Lambert-Beer law for the electric field E :

$$E(z) = E_0 e^{-\alpha z} \quad (5.5)$$

where α is the absorption coefficient and z the length of the medium. For the intensity this transforms into

$$I(z) = I_0 e^{-2\alpha z} = I_0 e^{-OD} \quad (5.6)$$

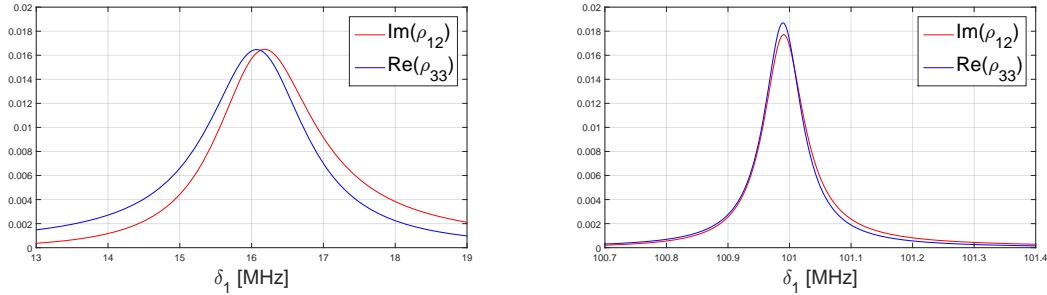
where OD is the optical depth of the system. The absorption coefficient α is related directly with the imaginary part of the electric susceptibility:

$$\alpha \propto \Im(\chi) \quad (5.7)$$

The absorption through the medium and therefore the amount of photons detected with the SPCM is proportional to the imaginary part of the susceptibility which is itself proportional to the coherence ρ_{21} :

$$\Im\chi \propto \rho_{21} \quad (5.8)$$

The detection via ionized Rydberg atoms however is clearly proportional to the population ρ_{33} of the Rydberg state $|3\rangle$.



(a) $\Im(\rho_{12})$ and $\Re(\rho_{33})$ for small frequency detuning (b) $\Im(\rho_{12})$ and $\Re(\rho_{33})$ for large frequency detuning

Figure 5.7: $\Im(\rho_{12})$ and $\Re(\rho_{33})$ for different frequency detunings. Only if the frequency detuning during the excitation is large enough, the position of ρ_{12} and ρ_{33} is the same.

Figure 5.7a and Figure 5.7b show the imaginary part of the coherence ρ_{21} and the real part of the population ρ_{33} for two different frequency detunings. Only if the detuning is large enough the position of ρ_{12} and ρ_{33} is the same which is a desired property for determining the MCP detection efficiency.

In the experiment the three-level system is of ladder-type as depicted in Figure 5.6 with the $5 S_{1/2}$ as the ground state, $5 P_{3/2}$ as the intermediate state and $66 S$ or $68 S$ for the Rydberg state.

To estimate the detection efficiency of the MCP the number of counted ionized Rydberg atoms has to be compared with the number of Rydberg excitations. The ability to count single photons with high accuracy allows us to estimate the number of Rydberg excitations and give together with the number of counted ions a lower limit for the MCPs detection efficiency.

The detection efficiency was determined in the transistor-sequence [GTS⁺14] where a coherent gate pulse containing on average one photon is sent into the cloud. In case of estimating the detection efficiency this ensures that no saturation effects of the MCP occur.

To calculate the average number of photons and thereby average number of Rydberg excitations the detection efficiency of the single-photon counting modules including losses at optical elements had to be calculated.

Figure 5.8 depicts a simplified schematic drawing of relevant probe laser optics and coupling into the SPCMs. The laser powers were measured with a powermeter at the positions 3, 7 and 8. Together with the transmission factors $T_{12} = 0.972$ and $T_{23} = 0.887$ the probe laser power at the position of the atom cloud can be calculated:

$$P_{\text{cloud}} = \frac{P_3}{T_{12} \cdot T_{23}} \quad (5.9)$$

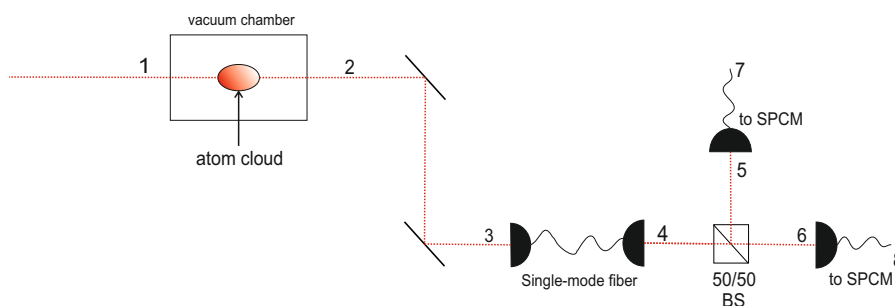


Figure 5.8: Simplified schematic drawing of the probe laser setup and coupling into SPCMs to calculate the detection efficiencies of both counters

The detection efficiencies for both single-photon counters are now given by:

$$\eta_{\text{SPCM}_1} = \frac{P_7}{P_{\text{cloud}}} \cdot \eta_q = 0.1668 \quad (5.10)$$

$$\eta_{\text{SPCM}_2} = \frac{P_8}{P_{\text{cloud}}} \cdot \eta_q = 0.1866 \quad (5.11)$$

where $\eta_q = 0.6$ is the quantum efficiency of the counters which is specified by the manufacturer. With these values the maximum number of Rydberg excitations can be estimated as follows:

$$n_{\text{Ryd}} = \left(\frac{\bar{n}_{\text{SPCM}_1}}{\eta_{\text{SPCM}_1}} + \frac{\bar{n}_{\text{SPCM}_2}}{\eta_{\text{SPCM}_2}} \right) \cdot T_e \quad (5.12)$$

$\bar{n}_{\text{SPCM}_{1/2}}$ denote the average number of counted photon events for the two single photon counters. As the detection is realized with a Hanbury-Brown-Twiss setup the number of counts for both single photon counters has to be summed. $T_e = 0.9$ gives the transmission in the excited state $|2\rangle$ as the excitation does not fully translate the population into the Rydberg state $|3\rangle$. With the estimate number of Rydberg excitations the MCP detection efficiency can now be calculated with the mean number of measured ion counts

$$\begin{aligned} \eta_{\text{MCP}} &= \frac{\bar{n}_{\text{ions,sig}} - \bar{n}_{\text{ions,ref}}}{n_{\text{Ryd}}} \\ &= 0.287 \end{aligned} \quad (5.13)$$

where $\bar{n}_{\text{ions,sig}}$ and $\bar{n}_{\text{ions,ref}}$ are the average number of ions in the signal and reference shot respectively. It should be again pointed out that this is only a lower bound for the detection efficiency and that the actual efficiency might be slightly higher.

To check the calculation for the MCP detection efficiency for consistency Figure 5.9 shows calculated detection efficiencies as well as amounts of signal and reference photons and ions over 25 excitation pulses during one experiment cycle.

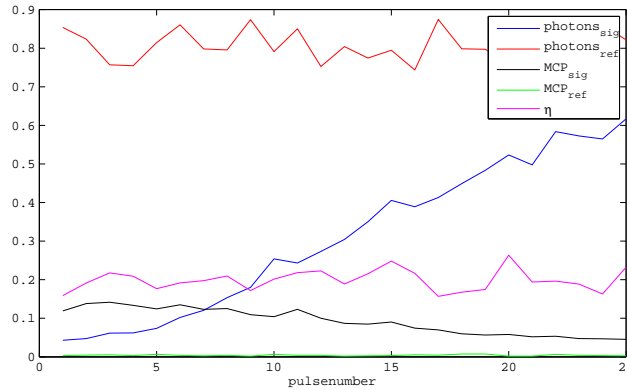


Figure 5.9: MCP detection efficiency and number of photons and ions respectively for different pulsenumbers

It can be clearly seen that the number of transmitted signal photons increases with higher pulsenumbers. This can be simply explained by an expanding of the atomic cloud due to the absent magneto-optical-trap leading to a high transmission according to the Lambert-Beer-law. Increasing photon transmission however means less effective Rydberg excitation which results in a decrease of detected ions with continuous pulsenumbers. As the calculated MCP detection efficiency stays constant within statistical fluctuations the presented calculation of the detection efficiency can be verified.

5.4 Stark Maps and electric field calibration

In this subsection the MCPs ion signal is used to calibrate stray electric field using Stark maps. Apart from that one measured Stark map is utilized to compare photon and ion signal regarding contrast and signal-to-noise ratio.

5.4.1 Stark Map 100 D-state

One attempt to calibrate the electric field was by taking stark maps in the 100 D-state. Due to an external magnetic field the zeeman sub-levels split resulting in several parabolas whose unambiguous assignment seems to be complicated. Although the resulting Stark map, shown in Figure 5.10 shall be used to compare the contrast as well as the signal-to-noise ratio of both photon and ion signal.

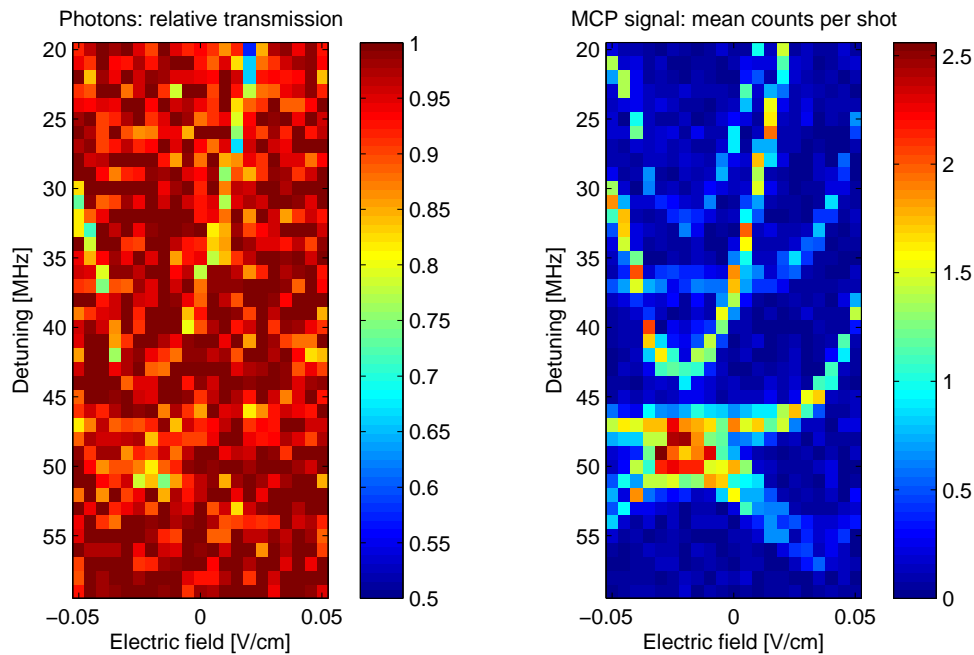


Figure 5.10: Stark map for the 100 D state. On the left relative transmission of photons was recorded for different detunings and electric field strengths. On the right the mean MCP ion signal is shown for different detunings and electric fields

To estimate the contrast and signal-to-noise ratio respectively, it was assumed that the fluctuations of a coherent light source obey Poissonian statistics as well as the number of ion counts fluctuates with a Poissonian distribution if the Rydberg-Rydberg interaction for example due to blockade effects is not strong enough to cause sub-poissonian statistics [LRBR05].

The probability distribution for n randomly distributed photons is then given by

$$P(n) = \frac{\langle n \rangle^n}{n!} e^{-\langle n \rangle} \quad (5.14)$$

where $\langle n \rangle$ denotes the expectation value of n . Fluctuations of the photon number around the expectation value are characterized in terms of the variance, which is defined as the square of the standard deviation. For a Poissonian distribution the variance $(\Delta n)^2$ is given by the expectation value $\langle n \rangle$, meaning that the variance is given by the mean number of photons. Assuming the same statistical properties for the number of ions they also obey to these characteristics.

The Michelson contrast or modulation is defined as

$$C = \frac{I_{max} - I_{min}}{I_{max} + I_{min}} \quad (5.15)$$

with $0 \leq C \leq 1$. In this case I_{max} is given by the maximum number of ion counts in case of the MCP signal and by the number of reference photons in case of the photon signal. I_{min} is then given by the mean number of ion counts. Regarding the photon signal I_{min} was assumed as the number of reference photons multiplied with a relative transmission of $T_{rel} = 0.8$. This value is only a read-off in Figure 5.10 giving the relative transmission at positions where the Stark parabolas occur.

The contrast for photon and MCP signal then follows as:

$$C_{\text{photons}} = \frac{n_{ref} \cdot (1 - T_{rel})}{n_{ref} \cdot (1 + T_{rel})} = 0.11 \quad (5.16)$$

$$C_{\text{ions}} = \frac{n_{max} - \bar{n}}{n_{max} + \bar{n}} = 0.96 \quad (5.17)$$

Another characteristic that specifies the resolution of both images is given by the signal-to-noise ratio SNR. In this case the signal-to-noise ratio can be defined as follows:

$$SNR = \frac{\langle n \rangle_{\text{Signal}}}{\langle n \rangle_{\text{Noise}}} \quad (5.18)$$

In case of the ion signal this turns into:

$$SNR_{\text{ions}} = \frac{n_{max} - \bar{n}}{\bar{n}} = 53.57 \quad (5.19)$$

$$= 30.36 \text{ dB} \quad (5.20)$$

In case of the photon signal the SNR is given by:

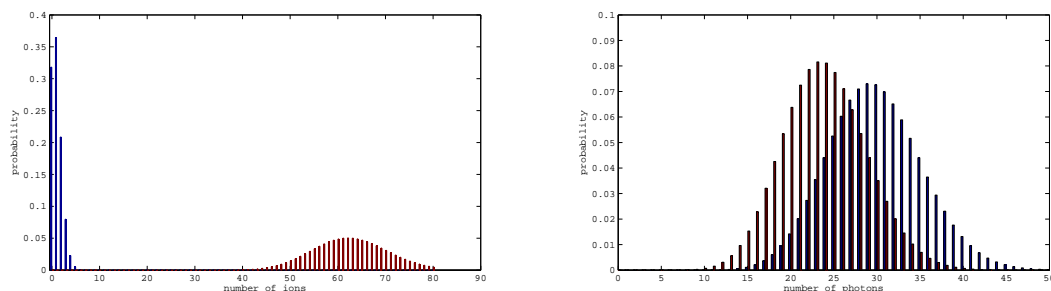
$$SNR_{\text{photons}} = \frac{\langle n \rangle_{ref} (1 - T_{rel})}{n_{ref} \cdot T_{rel}} = 0.25 \quad (5.21)$$

$$= 0.56 \text{ dB} \quad (5.22)$$

This fact can also be understood in a more graphical way. Figure 5.11a illustrates the Poissonian distributions for the maximum number of ion counts and the mean number of ion counts for 25 excitation pulses. Figure 5.11b shows the Poissonian distributions for the corresponding photon numbers denoting the number of reference photons and the number of transmitted photons that are given by 80 % of the number of reference photons for 25 excitation pulses.

If now the variance of the distribution that represents the noise is in the range of the mean signal the SNR is high compared to the case depicted in Figure 5.11a.

This means that the strong overlap of both distributions in Figure 5.11b gives a measure of the signal-to-noise ratio and therefore provides a rather intuitive method of comparing the contrast between both signals.



(a) Poissonian distributions for mean number of ion counts (blue) and maximum number of ion counts (red) (b) Poissonian distributions for number of reference photons (blue) and maximum number of transmitted photons (red)

Figure 5.11: Poissonian distributions for maximum ion respectively photon signal for 25 excitation pulses to estimate the contrast and signal-to-noise-ratio for photon and MCP signal

However, it has to be mentioned that the calculated values depend a lot on the probe and control laser intensities. For low control laser intensities the MCP signal is better than the photon signal as there is less absorption leading to a lower contrast. For high control powers however, there are regimes where the photon signal is clearer due to a higher absorption improving the signal-to-noise ratio. This can be explained as a higher control rabi frequency broadens the absorption line leading to a smaller blockade radius. Simultaneously a higher control rabi frequency can also destroy single Rydberg excitations due to decay processes to the intermediate state which results in a lower ion signal.

A physical explanation for the low contrast in case of the photon signal compared to the high contrast in case of the ion signal is the strong interaction in the $100 D$ state leading to a high blockade radius. This means that on average only a low amount of Rydberg atoms, perhaps three or four, can be simultaneously excited over the volume of the atom cloud. If the photon rate for the measurement is then too high and only a small amount of photons can be absorbed at all, the relative absorption is small. As the medium however is saturated with Rydberg atoms that can all be ionized, the contrast

regarding the ion signal is significantly higher.

5.4.2 Electric Field Calibration in 68 S-state

One of the main applications of the MCP during this thesis was to use the ion signal to eliminate stray electric fields by recording Stark maps. Therefore the ion signal was recorded for different frequency detunings as well as for different electric fields. Since Rydberg atoms in the 68 S state do not exhibit a permanent dipole moment they show quadratic Stark effect in the presence of an external electric field.

If no other field than the electric field applied with 4 electrodes in a specified configuration appeared, the vertex of the resulting parabola would be at zero electric field. However, due to the presence of stray electric fields, the vertex gets shifted to a nonzero value.

By adjusting the offset electric field the vertex of the stark parabola is pushed towards zero. This done by setting a constant electric field in the opposite direction to compensate these stray electric fields. The offset value is given by the displacement of the parabolas vertex.

After scanning the electric field in every direction the last scan serves as a control. This scan was done with a larger maximum electric field and is depicted in Figure 5.12.

It shows the mean number of ion counts for different frequency detunings and electric fields. On the right the frequency at the maximum number of ion counts for each electric field strength was taken to fit a parabola of the form:

$$\Delta(E) = \frac{1}{2}\alpha \cdot E^2 + c \quad (5.23)$$

where Δ is the frequency detuning and α the polarizability.

The theoretical value for the polarizability in 68 S state is $-217.4 \text{ MHz}/(\text{V}/\text{cm})^2$. After calibrating the stray electric fields to zero the last scan yields a polarizability of $-223.1 \text{ MHz}/(\text{V}/\text{cm})^2$ which is only 2.55 % off the theoretical value. This fit parameter was obtained in the fourth scan after taking Stark maps in x-, y- and z-direction. However stray electric fields only lead to a shift of the parabolas vertex and do not affect the curvature of the parabola. Therefore the other scans obtain similar results for the polarizability but the smaller scanning range of the electric field leads to a slightly higher deviation to the theoretical value.

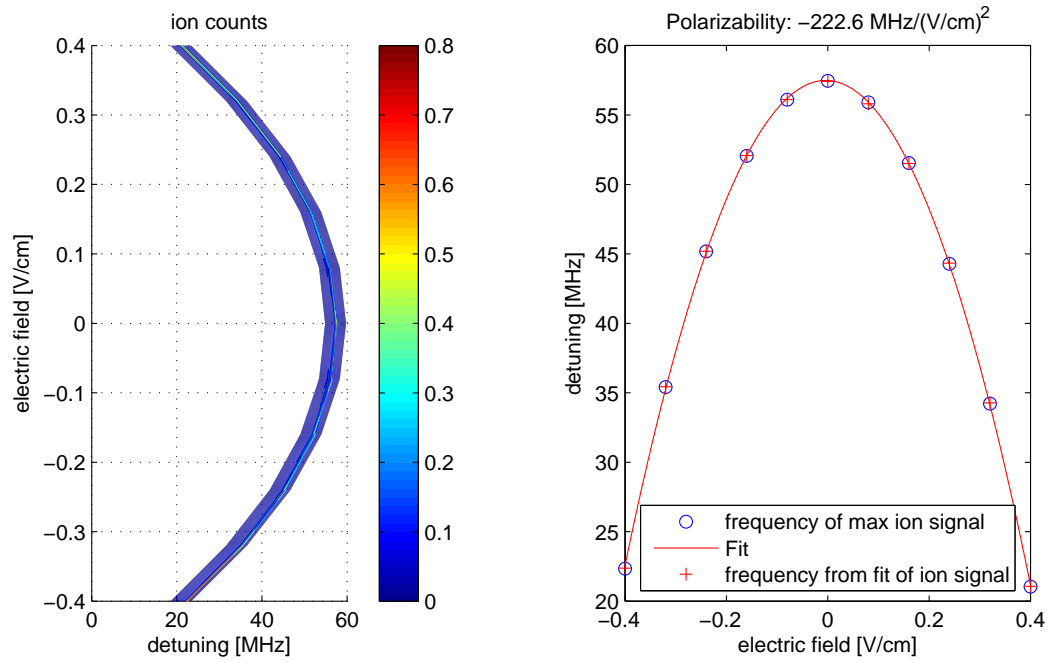


Figure 5.12: Stark map for the 68 S state. On the left mean ion counts for different detunings and electric field strengths. On the right frequency detuning vs. electric field with the frequency of maximum ion signal and the frequency resulting from a quadratic fit

6 Summary and Outlook

In this thesis first characterization measurements with a micro-channel-plate that has been integrated into the experiment and ion detection measurements including the work with the new electric field control have been presented.

Before starting with actual ion detection the program SIMION has been used to simulate electric fields to determine appropriate voltages that have to be set to achieve required electric fields in different coordinate directions. Apart from that SIMION could be used to simulate ion trajectories to determine guiding voltages for different ionization voltages and to investigate times of flight for different accelerations due to the ionization pulses. Furthermore hit points on the MCP have been simulated using SIMION.

In first ion detection measurements the full 500 V were used to ionize Rydberg atoms and to guide them with -120 V to the MCP. It has been shown that the ionization pulses lead to electric noise causing dark counts on the MCP. Therefore the actual ion signal had to be separated from the noise. The next attempt was to optimize steering voltages for different ionization voltages. Due to the diameter of the MCP a voltage range exists where it is possible to achieve a constant ion signal. This behaviour has been investigated and compared with theoretical simulations. It is surprising that the agreement with the theoretical data is remarkably good. In fact, the experimental data shows that the real voltage range where the MCP produces a nearly constant ion signal is even wider than what the simulations predict.

After optimizing all voltages the MCP detection efficiency has been estimated. Therefore the single-photon counting modules have been used to estimate the number of Rydberg excitations. With the number of Rydberg excitations and the number of detected ions a detection efficiency of 28.26 % could be achieved. However, this is of course only a lower bound as it assumes a perfect Rydberg excitation and the real detection efficiency should be higher. The obtained value is yet in the range of the specified detection efficiency from Hamamatsu which lies in between 5 and 58 % for ions with energies between 0.5 keV and 2 keV.

By taking Stark maps the quadratic Stark effect has been used to eliminate external stray electric fields by applying offset fields to shift the vertex of the Stark parabola to zero. This method of applying opposing electric fields has been repeated in every coordinate direction. Apart from that the signal-to-noise ratio as well as the noise of both ion and photon signal regarding a Stark map in the 100 D state with present magnetic fields have been estimated. It will be interesting to see how the stray fields fluctuate and therefore how often recalibrations of the offset electric fields have to be executed by taking Stark maps.

The next goal using electric field control and MCP will be a state-selective ionization using ionization ramps to successively ionize 68 S and 66 S states. These states will likely be used to increase the gain of the single-photon transistor making use of Förster resonances [NBK⁺12]. It should be in principle possible to separate the ion signal of both states due to their slightly differing times of flight which can be increased by the time difference where the ionization voltages reach the respective thresholds. This can be for example realized by integrating another RC-circuit after the HV-switch to ramp

the ionization voltage exponentially.

Summing up, the calibration and characterization of a micro-channel-plate has been executed integrating a second detection method to the experiment which can be used complement to the single-photon counting modules. Furthermore the electric field control has been tested and calibrated with Rubidium atoms in the cloud.

7 Appendix

List of Figures

2.1	Dependence of the polarizability α on the effective principle quantum number n^* extracted from experimental data [OS85]. The results are in good agreement with perturbative calculations	5
2.2	The classical coulomb potential $\propto -\frac{1}{r}$ (red) gets modified to an effective potential $\propto -\frac{1}{r} - E \cdot r$ (blue) by an electric potential (green) $\propto -E \cdot r$. The modification of the potential leads to a saddle point. Rydberg electrons with a binding energy below the energy of the saddle-point can no longer be bound and get ionized	6
3.1	Autodesk Inventor drawing of the electric field control with 8 independent electrodes in a cloverleaf configuration and two electrodes to guide ionized Rydberg atoms. 11-13 denote mesh and MCP.	8
3.2	Schematic drawing and allocation of control voltages on the individual field plates.	9
3.3	Structure and operating principle of micro-channel plates [Ham]	10
3.4	Operating principle of the MCP: an incident electron striking the channel wall and producing a secondary electron which also follows a parabolic trajectory due to the electric field applied between the MCP channel electrodes. This process is repeated several times leading to a large amount of output electrons.	10
3.5	Cross section of a two stage and three stage MCP assembly indicating the bias angle between channel axis and the axis perpendicular to the plates surface	11
3.6	MCP traces from random events with amplifier ZX-14012L-S+ from Mini-Circuits	12
3.7	FPGA based Time-Tagger with 8 independent channels for time-resolved counting of digital pulses	13
4.1	Electric fields generated by setting a positive voltage on electrodes 2 and 6 and a negative voltage on electrodes 4 and 8	15
4.2	Electric fields generated by setting a positive voltage on electrodes 1 and 5 and a negative voltage on electrodes 3 and 7	15
4.3	Electric fields generated by setting a positive voltage on electrodes 1 and 3 and a negative voltage on electrodes 5 and 7	15
4.4	Simulated ion trajectory for 100 $^{87}\text{Rb}^+$ ions distributed in a sphere with a diameter of 200 μm in the center of symmetry. The ionization voltage on electrodes 2 and 6 was set to +500 V, the steering voltage on electrode 9 to -100 V.	16
4.5	Simulated hit statistics of ions impinging the MCP. For the simulation 100 $^{87}\text{Rb}^+$ ions distributed in a sphere of the size of the atom cloud were used. The ionization voltage was chosen to be +100 V. The coordinates are SIMION coordinates.	18

5.1	MCP dark counts for different trigger levels (left) and MCP pulse-height-distribution (right)	20
5.2	count rate at low trigger levels to investigate the influence of Rb dispensers and ionization gauge on the dark count statistics	21
5.3	Ion signal for two different ionization voltages. The two high peaks are a crosstalk signal resulting from the voltage applied to ionize Rydberg atoms. The actual ion signal is given by the small peak between the crosstalk.	22
5.4	Ion signal for two different scans of the steering voltage.	23
5.5	Three linear fits for different impinging points on the MCP. Green: ions impinging left side of MCP, red: ions impinging right side of MCP, blue: ions impinging center of MCP	24
5.6	Ladder-type atomic 3-level system used in the experiment. The ground state $ 1\rangle$ is given $5 S_{1/2}$, the $5 P_{3/2}$ level is used for the intermediate state $ 2\rangle$ and the $66 S$ or $68 S$ for the Rydberg state $ 3\rangle$	25
5.7	$\Im(\rho_{12})$ and $\Re(\rho_{33})$ for different frequency detunings. Only if the frequency detuning during the excitation is large enough, the position of ρ_{12} and ρ_{33} is the same.	27
5.8	Simplified schematic drawing of the probe laser setup and coupling into SPCMs to calculate the detection efficiencies of both counters	28
5.9	MCP detection efficiency and number of photons and ions respectively for different pulsenumbers	29
5.10	Stark map for the 100 D state. On the left relative transmission of photons was recorded for different detunings and electric field strengths. On the right the mean MCP ion signal is shown for different detunings and electric fields	31
5.11	Poissonian distributions for maximum ion respectively photon signal for 25 excitation pulses to estimate the contrast and signal-to-noise-ratio for photon and MCP signal	33
5.12	Stark map for the 68 S state. On the left mean ion counts for different detunings and electric field strengths. On the right frequency detuning vs. electric field with the frequency of maximum ion signal and the frequency resulting from a quadratic fit	35

References

- [BTRD14] BAUR, Simon ; TIARKS, Daniel ; REMPE, Gerhard ; DÜRR, Stephan: Single-Photon Switch Based on Rydberg Blockade. In: *Phys. Rev. Lett.* 112 (2014), Feb, 073901. <http://dx.doi.org/10.1103/PhysRevLett.112.073901>. – DOI 10.1103/PhysRevLett.112.073901
- [DK12] DUDIN, Y. O. ; KUZMICH, A.: Strongly Interacting Rydberg Excitations of a Cold Atomic Gas. In: *Science* 336 (2012), Nr. 6083, 887–889. <http://dx.doi.org/10.1126/science.1217901>. – DOI 10.1126/science.1217901
- [FIM05] FLEISCHHAUER, Michael ; IMAMOGLU, Atac ; MARANGOS, Jonathan P.: Electromagnetically induced transparency: Optics in coherent media. In: *Review of Modern Physics* 77 (2005), April
- [FS82] FEYNMAN, Richard ; SHOR, Peter W.: Simulating Physics with Computers. In: *SIAM Journal on Computing* 26 (1982), S. 1484–1509
- [GTS⁺14] GORNIACZYK, Hannes ; TRESP, Christoph ; SCHMIDT, Johannes ; FEDDER, Helmut ; HOFFERBERTH, Sebastian: *Single Photon Transistor Mediated by Inter-State Rydberg Interaction*. <http://dx.doi.org/10.1103/PhysRevLett.113.053601>. Version: April 2014
- [Ham] HAMAMATSU: *MCP & MCP Assembly, Selection Guide*
- [HLW⁺11] HONER, Jens ; LÖW, R. ; WEIMER, Hendrik ; PFAU, Tilman ; BÜCHLER, Hans P.: Artificial Atoms Can Do More Than Atoms: Deterministic Single Photon Subtraction from Arbitrary Light Fields. In: *Phys. Rev. Lett.* 107 (2011), Aug, 093601. <http://dx.doi.org/10.1103/PhysRevLett.107.093601>. – DOI 10.1103/PhysRevLett.107.093601
- [JCZ⁺00] JAKSCH, D. ; CIRAC, J. I. ; ZOLLER, P. ; ROLSTON, S. L. ; CÔTÉ, R. ; LUKIN, M. D.: Fast Quantum Gates for Neutral Atoms. In: *Phys. Rev. Lett.* 85 (2000), Sep, 2208–2211. <http://dx.doi.org/10.1103/PhysRevLett.85.2208>. – DOI 10.1103/PhysRevLett.85.2208
- [LFC⁺01] LUKIN, M. D. ; FLEISCHHAUER, M. ; COTE, R. ; DUAN, L. M. ; JAKSCH, D. ; CIRAC, J. I. ; ZOLLER, P.: Dipole Blockade and Quantum Information Processing in Mesoscopic Atomic Ensembles. In: *Phys. Rev. Lett.* 87 (2001), Jun, 037901. <http://dx.doi.org/10.1103/PhysRevLett.87.037901>. – DOI 10.1103/PhysRevLett.87.037901
- [LRBR05] LIEBISCH, T. C. ; REINHARD, A. ; BERMAN, P. R. ; RAITHEL, G.: Atom Counting Statistics in Ensembles of Interacting Rydberg Atoms. In: *Phys. Rev. Lett.* 95 (2005), Dec, 253002. <http://dx.doi.org/10.1103/PhysRevLett.95.253002>. – DOI 10.1103/PhysRevLett.95.253002

- [LWN⁺12] LÖW, Robert ; WEIMER, Hendrick ; NIPPER, Johannes ; BALEWSKI, Jonathan B. ; BUTSCHER, Björn ; BÜCHLER, Hans P. ; PFAU, Tilman: An experimental and theoretical guide to strongly interacting Rydberg gases. In: *Journal of Physics B: Atomic, Molecular and Optical Physics* 45 (2012), Nr. 11, S. 113001
- [NBK⁺12] NIPPER, J. ; BALEWSKI, J. B. ; KRUPP, A. T. ; BUTSCHER, B. ; LÖW, R. ; PFAU, T.: Highly Resolved Measurements of Stark-Tuned Förster Resonances between Rydberg Atoms. In: *Phys. Rev. Lett.* 108 (2012), Mar, 113001. <http://dx.doi.org/10.1103/PhysRevLett.108.113001>. – DOI 10.1103/PhysRevLett.108.113001
- [OS85] O’SULLIVAN ; STOICHEFF: Scalar polarizabilities and avoided crossings of high Rydberg states in Rb. In: *Phys. Rev., A* 31 (1985), April, Nr. 4, S. 2718–2720
- [PFL⁺12] PEYRONEL THIBAUT ; FIRSTENBERG OFER ; LIANG QI-YU ; HOFFERBERTH SEBASTIAN ; GORSHKOV ALEXEY V. ; POHL THOMAS ; LUKIN MIKHAIL D. ; VULETIC VLADAN: Quantum nonlinear optics with single photons enabled by strongly interacting atoms. In: *Nature* 488 (2012), aug, Nr. 7409, 57–60. <http://dx.doi.org/10.1038/nature11361>. – DOI 10.1038/nature11361. – ISSN 0028–0836. – 10.1038/nature11361
- [PMG⁺10] PRITCHARD, J. D. ; MAXWELL, D. ; GAUGUET, A. ; WEATHERILL, K. J. ; JONES, M. P. A. ; ADAMS, C. S.: Cooperative Atom-Light Interaction in a Blockaded Rydberg Ensemble. In: *Phys. Rev. Lett.* 105 (2010), Nov, 193603. <http://dx.doi.org/10.1103/PhysRevLett.105.193603>. – DOI 10.1103/PhysRevLett.105.193603
- [Sch07] SCHWABL, F.: *Quantenmechanik*. Berlin : Springer-Verlag, 2007 <http://link.springer.com/book/10.1007%2F978-3-540-73675-2>. – ISBN 978–3–540–73675–2
- [Sch14] SCHMIDT, Johannes: *Generation of non-classical light using ultra-cold Rydberg ensembles*. Germany, University of Stuttgart, Master thesis, October 2014
- [WS08] WALKER, Thad G. ; SAFFMAN, M.: Consequences of Zeeman degeneracy for the van der Waals blockade between Rydberg atoms. In: *Phys. Rev. A* 77 (2008), Mar, 032723. <http://dx.doi.org/10.1103/PhysRevA.77.032723>. – DOI 10.1103/PhysRevA.77.032723
- [ZMHZ10] ZHAO, Bo ; MÜLLER, Markus ; HAMMERER, Klemens ; ZOLLER, Peter: Efficient quantum repeater based on deterministic Rydberg gates. In: *Phys. Rev. A* 81 (2010), May, 052329. <http://dx.doi.org/10.1103/PhysRevA.81.052329>. – DOI 10.1103/PhysRevA.81.052329